

ARTICLE OPEN



Origins of Southern Ocean warm sea surface temperature bias in CMIP6 models

Fengyun Luo^{1,2}, Jun Ying^{2,3}✉, Tongya Liu^{2,3} and Dake Chen^{1,2,3}✉

The warm sea surface temperature (SST) bias in the Southern Ocean (SO) has persisted in several generations of Coupled Model Inter-comparison Project (CMIP) models, yet the origins of such a bias remain controversial. Using the latest CMIP6 models, here we find that the warm SST bias in the SO features a zonally oriented non-uniform pattern mainly located between the northern and southern fronts of the Antarctic Circumpolar Current. This common bias is not likely to be caused by the biases in the surface heat flux or the strength of the Atlantic meridional overturning circulation (AMOC) — the two previously suggested sources of the SO bias based on CMIP5 models. Instead, it is linked to the robust common warm bias in the Northern Atlantic deep ocean through the AMOC transport as an adiabatic process. Our findings indicate that remote oceanic biases that are dynamically connected to the SO should be taken into account to reduce the SO SST bias in climate models.

npj Climate and Atmospheric Science (2023)6:127; <https://doi.org/10.1038/s41612-023-00456-6>

INTRODUCTION

Characterized by the Antarctic Circumpolar Current (ACC)—a dominant part of the global thermohaline circulation—the Southern Ocean (SO) plays a unique and key role in the global climate system^{1–3}. It not only zonally connects three ocean basins—the Pacific, the Atlantic, and the Indian Ocean, but also vertically links the sea surface temperature (SST) with the ocean interior by bringing up deep water through the westerly wind-driven divergence. Normally, the deep water in the SO, consisting of the Northern Atlantic Deep Water (NADW) of high salinity and high oxygen concentration, upwells along the isopycnal^{1,4} to the sea surface⁵. One part of the surface flow travels northward to form the Subantarctic Mode Water and Antarctic Intermediate Water (AAIW), while the other moves southward and sinks to be part of the Antarctic Bottom Water⁶. The SO dynamics is critical in anthropogenic carbon and heat uptake and in redistributing global energy^{7–9}. Therefore, understanding the basic state of the SO is among the most important tasks in climate change research. As sustained SO observations are lacking¹⁰, numerical simulations based on coupled climate models are an indispensable and essential way to study the SO.

However, the SO has persistently suffered a systematic warm SST bias in several generations of climate models participating in the Coupled Model Inter-comparison Project (CMIP)^{11–13}. This warm bias appears as one of the most prominent biases in global SST modeling¹², precluding correct simulations of the current climate such as the location of the inter-tropical convergence zone¹⁴, the recent trend of the Southern Annual Mode (SAM)¹⁵, and the response of SO SST to SAM¹⁶. Moreover, it also lowers the reliability of model projections for future climate change¹⁷.

A few previous studies have proposed possible causes of the SO warm SST bias in CMIP models. For instance, ref. ¹² found in a large set of CMIP5 models, that the models with a weaker Atlantic Meridional Overturning Circulation (AMOC) tend to have warmer SST in the SO, and thus the common SO warm SST bias can be attributed to an overly weak AMOC strength. In contrast, ref. ¹⁸ revealed an extremely weak inter-model correlation between the

AMOC strength and the SO SST among CMIP5 models. Instead, they found the surface shortwave radiation is more responsible for the diversified simulations of SO SST and claimed that the warm SST bias in the SO is primarily caused by the overestimation of cloud-related shortwave radiation. These two contradictory explanations obscure a clear judgment of the true source of the common SO warm SST bias.

The warm SST bias anchored in the SO is still prevailing in the latest sixth phase of CMIP (CMIP6) models (Fig. 1a), and the magnitude of such a bias is comparable to those in the previous generations of CMIP models^{11,12}, even though there are generally higher spatial resolutions and more reasonable physical parameterizations in CMIP6 models than in their predecessors¹⁹. Moreover, the bias of surface downward shortwave radiation has been revealed to be largely remediated²⁰ and the AMOC has been shown to be reasonably simulated^{21,22} in CMIP6 models. All these raise a natural question: are the causes suggested to be responsible for the common SO warm SST bias among CMIP5 models still working in CMIP6 models? If not, what are the origins of this persistent common warm SST bias in CMIP6 models?

RESULTS

SST bias in the SO

The CMIP6 multi-model mean (MMM) SST bias in the SO displays a zonally nonuniform band-like warm pattern (Fig. 1a). The warm biases are more robust and consistent in the Indian and Atlantic Ocean sectors and weaker in the Pacific Ocean sector, which are similar to the zonal distributions of the common SO warm SST bias in the CMIP3 and CMIP5 models (see Fig. 5a in ref. ¹¹ and Fig. 1a in ref. ¹², respectively). Overlaying the observed circumpolar Subantarctic Front (SAF) and the southern Antarctic Circumpolar Current Front (SACCF) (see Methods), we find that the warm SST bias in the MMM, as well as in most individual models, is mainly confined within these two ACC fronts (black lines in Fig. 1a; Supplementary Fig. 1).

¹Ocean College, Zhejiang University, Zhoushan, China. ²State Key Laboratory of Satellite Ocean Environment Dynamics, Second Institute of Oceanography, Ministry of Natural Resources, Hangzhou, China. ³Southern Marine Science and Engineering Guangdong Laboratory (Zhuhai), Zhuhai, China. ✉email: yingjun@sio.org.cn; dchen@sio.org.cn

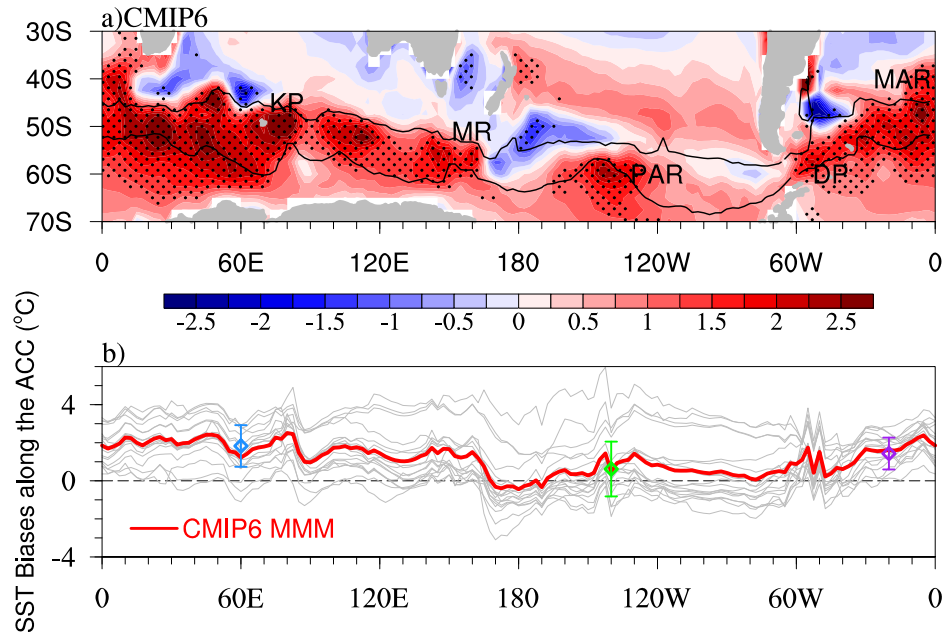


Fig. 1 Southern Ocean (SO) SST biases. **a** The multi-model mean (MMM) SST bias (units: $^{\circ}\text{C}$) in the SO. Black lines are the observational northern (SAF, -0.035 dym) and southern (SACCF, 0.985 dym) boundaries of the ACC, which are defined by AVISO combined mean dynamic topography (MDT_CNES_CLS13) according to Kim and Orsi (2014). Stippling indicates areas where more than 80% of models agree on the sign of bias. The labels in **(a)** indicate prominent topographic features, including the Kerguelen Plateau (KP), the Macquarie Ridge (MR), the Pacific–Antarctic Ridge (PAR), the Drake Passage (DP), and the Mid-Atlantic Ridge (MAR). **b** The meridional averaged SST biases within SAF and SACCF for each model (gray lines) and CMIP6 MMM (red line). The colored error bars and diamond boxes denote the MMM SST bias and the standard deviations, from left to right, for the Indian Ocean sector (blue), the Pacific Ocean sector (green), and the Atlantic Ocean sector (purple).

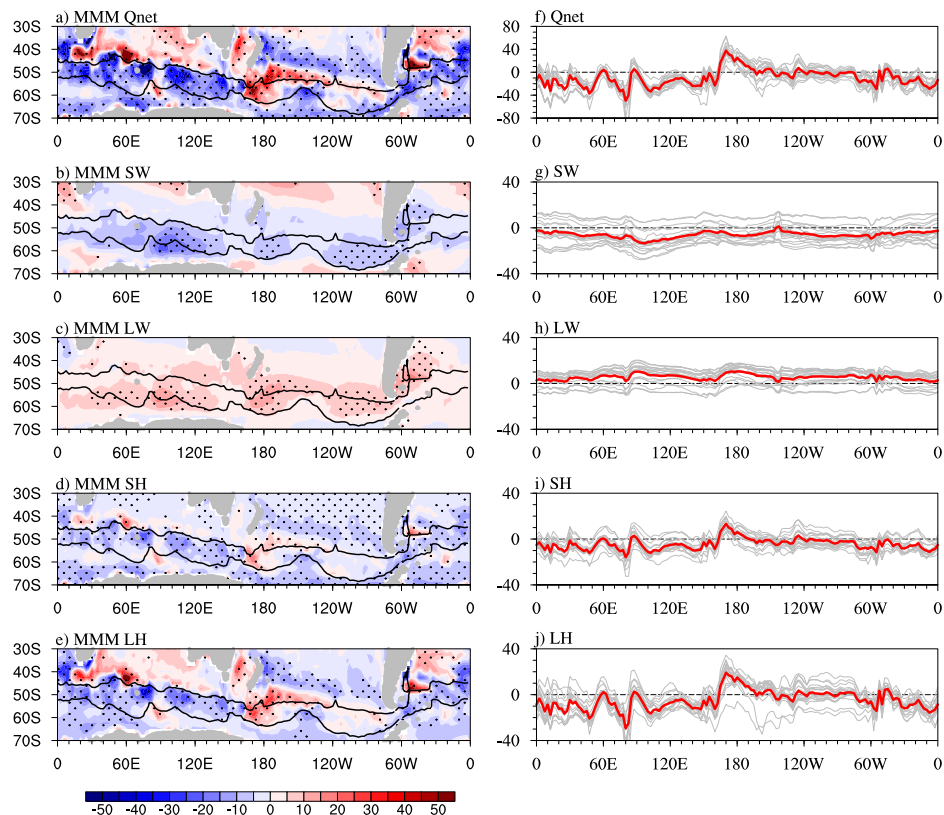


Fig. 2 Surface heat flux biases. The left column is the MMM spatial patterns of **(a)** net heat flux (Qnet) bias, **(b)** shortwave radiation (SW) bias, **(c)** longwave radiation (LW) bias, **(d)** sensible heat flux (SH) bias, and **(e)** latent heat flux (LH) bias. The two black lines in **(a–e)** are same as in Fig. 1. Stippling indicates areas where more than 80% of models agree on the sign of bias. The right column is the meridional-averaged **(f)** Qnet biases, **(g)** SW biases, **(h)** LW biases, **(i)** SH biases, **(j)** LH biases (units: W m^{-2}) for individual models (gray lines) and MMM (bold red lines). The sign of surface heat flux terms is positive when going downward.

The zonally nonuniform SST bias pattern is to some extent associated with the complex topographies in the SO (Fig. 1a). For instance, extreme warm biases appear in the Kerguelen Plateau, the Macquarie Ridge, the Pacific–Antarctic Ridge, the Drake Passage, and the Mid-Atlantic Ridge. These biases coincide with the hot spots in the SO, including the steepening isopycnals, intensified eddy activities, enhanced cross-front eddy heat exchanges, and facilitated upwelling of deep water^{3,23,24}. In addition, there are also some regional cold SST biases in the eastern boundary current areas, probably arising from model deficiencies in simulating these currents and associated local dynamics. The origins of these regional SST biases cannot be ascertained since variables essential to study the corresponding subgrid-scale processes are unavailable from climate models. Thus our focus here is to explore the origins of the common warm SST bias in the SO from the perspective of large-scale thermodynamics and dynamics.

By averaging the SST biases between the two observational ACC fronts (Fig. 1b), it again appears that the warm SST biases in the Atlantic and Indian sectors (reaching up to $\sim 2^\circ\text{C}$ in MMM) are stronger than that in the Pacific sector ($\sim 1^\circ\text{C}$ in MMM). The inter-model standard deviation (STD) of SST bias in the Pacific sector is almost twice as much as those in the Indian and Atlantic sectors, indicating higher inter-model consistency of the warm SST bias in the latter two than in the former (Fig. 1b, colored error bars). The weak inter-model consistency in the Pacific sector is mainly

caused by four models (EC-Earth3, EC-Earth3-Veg, MIRCO6, and MIRCO-ES2L) with extreme warm biases, which show larger warm biases in the whole SO than other models.

Effect of surface heat flux

Firstly we examine the biases of surface heat fluxes and their role in causing the common SO warm SST bias. Compared with the net surface heat flux (Q_{net} , positive downward) from ECMWF Reanalysis v5 (ERA5) dataset, the CMIP6 MMM Q_{net} displays an overall negative bias over the SO with high inter-model consistency (Fig. 2a, f), which generally opposes the positive MMM SST bias, with the spatial correlation between the two reaching up to -0.70 between 40°S and 60°S . This indicates that the Q_{net} bias does not contribute to the common warm SST bias in the SO but actually responds to it. For further verification, we choose six additional observational/reanalysis Q_{net} products to compute the MMM Q_{net} bias (Supplementary Fig. 2). The results show consistent negative Q_{net} biases, though the magnitude of the bias varies from one another due to observational uncertainties²⁵.

By decomposing the Q_{net} bias into biases of different flux terms, it becomes clear that the MMM shortwave radiation (SW) displays a totally negative bias over the SO (Fig. 2b), whereas the surface longwave radiation (LW) exhibits a positive bias that nearly counterbalances the bias of SW (Fig. 2c). In addition, both the MMM surface sensible heat flux (SH) and latent heat flux (LH) have

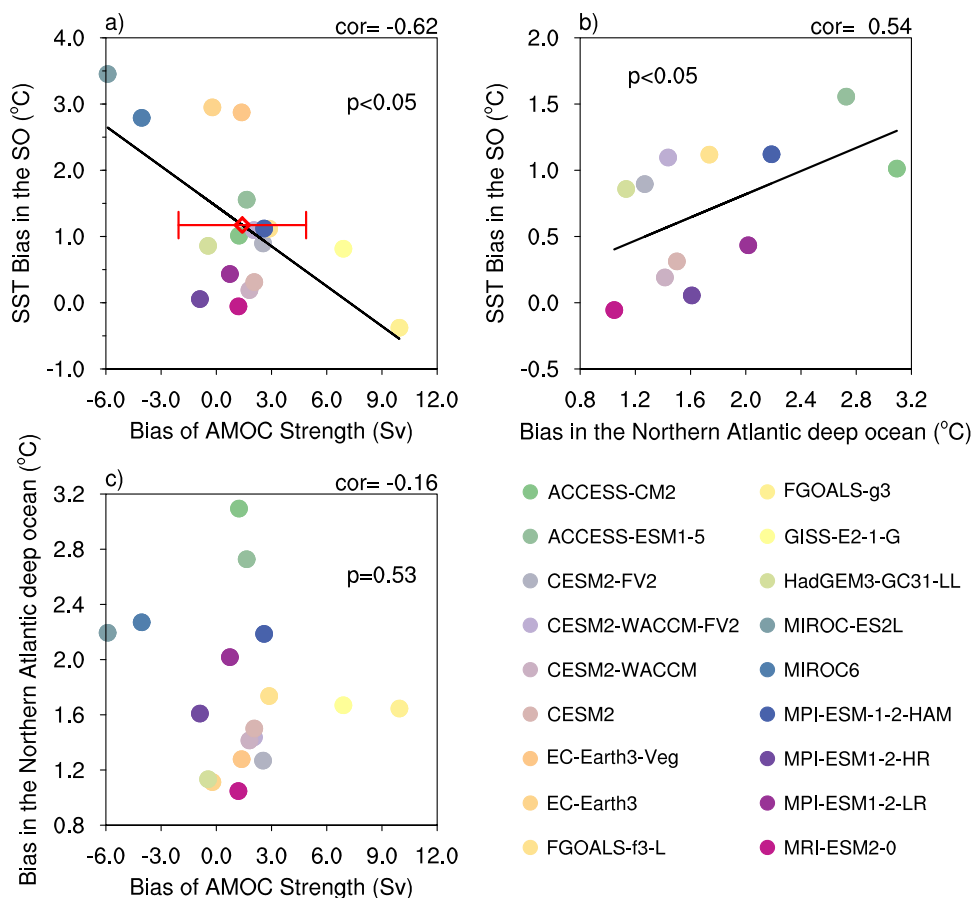


Fig. 3 Inter-model relationships. **a** Inter-model relationship between AMOC strength biases (units: Sv) and SST biases in the SO. Here the AMOC strength is defined as the maximum value of the meridional overturning streamfunction in the Atlantic Ocean at 26°N . The red diamond box denotes the MMM AMOC strength bias, and the red error bar is one standard deviation of the 18 models. **b** Inter-model relationship between Northern Atlantic ($30\text{--}60^\circ\text{N}, 70^\circ\text{W}\text{--}20^\circ\text{E}$) deep ocean ($1000\text{--}3000\text{ m}$) temperature biases and SST biases in the SO for models with reasonable AMOC strength. **c** Inter-model relationship between AMOC strength biases and Northern Atlantic deep ocean warm biases. The solid black line denotes the linear regression, and the correlation coefficient and the p value determined by a two-side Student's t test are also shown in each panel.

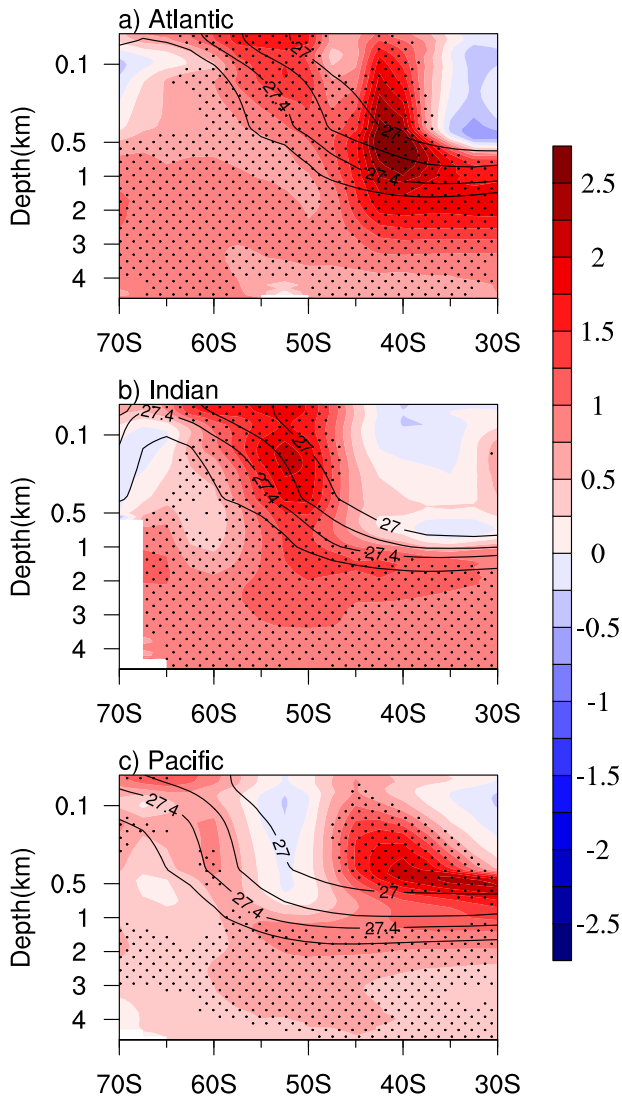


Fig. 4 Zonal mean temperature biases in three ocean sectors. Multi-model mean (MMM) zonally averaged ocean temperature biases (units: °C) in (a) Atlantic (70°W–20°E), (b) Indian (20°E–160°E), and (c) Pacific (160°E–70°W) ocean sectors. The black contours in each plot are the MMM potential density (units: kg m^{-3} , with interval 0.2 kg m^{-3}). Stippling indicates areas where more than 80% of models agree on the sign of bias.

negative biases between the two ACC fronts with similar spatial patterns but of different magnitudes (Fig. 2d, e). This indicates that the negative bias of Q_{net} is mainly due to turbulent heat flux biases, which release more heat from the ocean surface to balance the warm SST bias. Moreover, the negative bias of LH is stronger than that of SH, implying a dominant role of LH bias in responding to the warm SST bias. Most of the CMIP6 models yield the same results as the MMM (Fig. 2g–j), except for the two outliers with extreme warm SST bias in the SO, EC-Earth3-Veg and EC-Earth3, which show positive SW biases over the whole SO (Supplementary Fig. 3).

Effect of AMOC strength

Next, we turn to the effect of AMOC strength on the SO SST bias. Here and in the following analysis, the SO SST bias in each CMIP6 model is represented by the area-averaged SST bias between the observational SAF and SACCF, unless otherwise specified. As shown in Fig. 3a, there appears to be a significant negative inter-

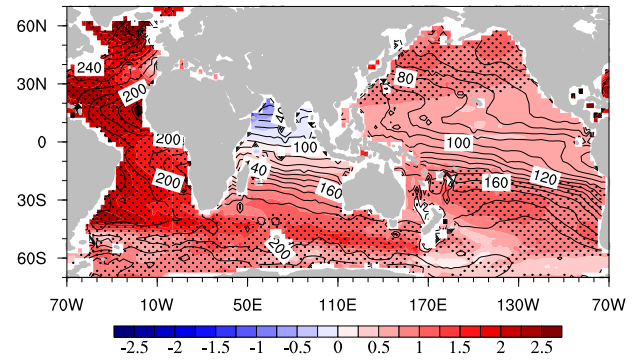


Fig. 5 Deep ocean temperature biases. Multi-model mean (MMM) ocean temperature biases (units: °C, shading) averaged between the depths of 1000 m and 3000 m. The black contours are the MMM climatological dissolved oxygen concentration ($\mu\text{mol kg}^{-1}$) at the same depth. Stippling indicates areas where more than 80% of models agree on the same sign of bias.

model relationship between the SO SST bias and the AMOC strength among 18 CMIP6 models, consistent with the result from CMIP5 multi-models¹², with weaker AMOC strength tending to have stronger warm SST bias. However, more than 70% of the chosen models have positively biased AMOC strength, and the MMM bias of AMOC strength is also slightly positive (1.41 Sv, red diamond in Fig. 3a). This implies that the common SO warm SST bias cannot be caused by the common bias of AMOC strength.

There are four models with their AMOC strength exceeding one inter-model STD. Two of them (FGOALS-g3 and GISS-E2-1-G) have their AMOC much stronger than the MMM while the other two (MIRCO-ES2L and MIRCO6) much weaker. It seems that only for these models with largely biased AMOC strength, there exists a strong negative correlation between the biases of AMOC strength and SO SST. If these four models are excluded from the model ensemble, the inter-model correlation coefficient between the bias of AMOC strength and that of SO SST reduces to as low as -0.04 . Thus, the effect of AMOC strength on the SO SST is highly model-dependent, which may explain the conflicting arguments regarding the role of weakening AMOC strength in causing the SO warm SST bias^{12,18}.

Effect of warm bias in the Northern Atlantic deep ocean

In the absence of a systematic AMOC strength bias that accounts for the common SO warm SST bias, together with a generally reasonable representation of surface heat flux and wind stress over the SO in CMIP6 models²⁶ (Supplementary Fig. 4), we turn to remote factors and find that the common warm bias in the deep Northern Atlantic could be partly responsible for the common SO warm SST bias through AMOC transport. As shown in Fig. 4, the MMM zonally-averaged ocean temperatures in all three ocean sectors show overall warm biases throughout the water column with somewhat similar spatial patterns. Larger biases appear in the deep ocean and clime upward and southward to the upper ocean nearly along the isopycnals (Fig. 4), indicating a deep source of bias from the north. The warm biases in the Atlantic sector generally appear in the NADW, where salinity exceeds 34.7 psu (Supplementary Fig. 5), rather than in the AAMW/AAIW.

The global deep ocean temperature bias averaged from 1000 m to 3000 m reveals that the largest warm bias is located in the Atlantic Ocean, and the warm biases in the SO gradually decrease from offshore of Argentina in the Atlantic Ocean sector to the east (Fig. 5). Such a spatial distribution of the global deep ocean warm bias resembles that of the dissolved oxygen concentration (black contours in Fig. 5), which is often used as an indicator for the

transport of NADW starting from the deep convective region in the Northern Atlantic Ocean²⁷. This implies that the warm bias in the North Atlantic deep ocean can be advected almost adiabatically to the surface of the SO, contributing to the warm SST bias there. Indeed, as shown in Fig. 3b, all of the models have a warm bias in the Northern Atlantic deep ocean (30–60°N, 70°W–20°E, 1000–3000 m), and the models with larger warm bias in the Northern Atlantic deep ocean tend to have larger SO warm SST bias (Fig. 3b), with a significant correlation of 0.54 (two-sided Student's *t* test, $p < 0.05$). The warm bias in the Northern Atlantic deep ocean is not linked to the bias of AMOC strength, since there is no significant correlation between the two (Fig. 3c).

To further demonstrate the processes through which the warm bias in the Northern Atlantic deep ocean impacts the SO warm SST bias, we perform a set of idealized model experiments with passive-tracer (see Methods). After tracers are released through the entire water column in the northern Atlantic Ocean (north of 60°N), they travel with the deep flow and arrive at the SO in about 200 years (Supplementary Fig. 6), and finally upwell to the surface (Fig. 6). The experimental results show that high concentrations at the surface are primarily confined to the SO (Fig. 6a–c), whereas higher concentrations in the deep ocean are in the Atlantic Ocean (Fig. 6d–f), which is very similar to the distribution of warm bias in the deep ocean shown in Fig. 5. Additionally, the zonal mean vertical structures of the tracer concentration also bear resemblance to that of the warm bias shown in Fig. 4, with the largest concentration located at depths about 1000–3000 m declining from the north to south (Fig. 7). These idealized passive-tracer experiments confirm that the common Northern Atlantic deep ocean warm bias can significantly contribute to the common warm SST bias in the SO.

DISCUSSION

Our analyses reveal that the biases of the net surface heat flux and the AMOC strength, which have been suggested to be the primary causes for the warm SST bias in the SO for CMIP5 models, are not the reasons for the same persistent warm bias in CMIP6 models. Instead, the remote warm bias in the Northern Atlantic deep ocean is found to be conducive for the common warm SST bias in the SO through adiabatic transport by AMOC, based on a large ensemble of climate model outputs, various observation/reanalysis datasets, as well as a series of idealized model experiments with passive-tracers. This remote transport of warm bias to the SO is similar, to some extent, to the southward propagation of excessive anthropogenic warming from the deep layer of Nordic Sea to the Southern Atlantic²⁸. The cause of the NADW warm bias is still unclear, but might be tied to the bias in ocean dynamics, such as unrealistic simulation of deep ocean convection, which will be explored in the future.

It should be noted, however, that the remote common warm bias in the North Atlantic deep ocean can only explain about 30% of the total inter-model variance of the SO SST bias, implying that there must be other causes of the SO warm SST bias remaining to be revealed. For example, the incorrect model representation of ocean eddy fluxes due to coarse spatial resolution could be important for the warm SST bias in the eddy-rich SO. Moreover, regional factors such as complicated local topography that strongly modulate the spatial pattern of the SO warm SST bias, are not considered within the current large-scale framework. Nevertheless, the warm bias in the Northern Atlantic deep ocean, which has been persistently present in almost all CMIP5 and CMIP6 models^{22,29}, as well as in climate models with higher spatial resolution²², have to be taken into account to reduce the SO bias,

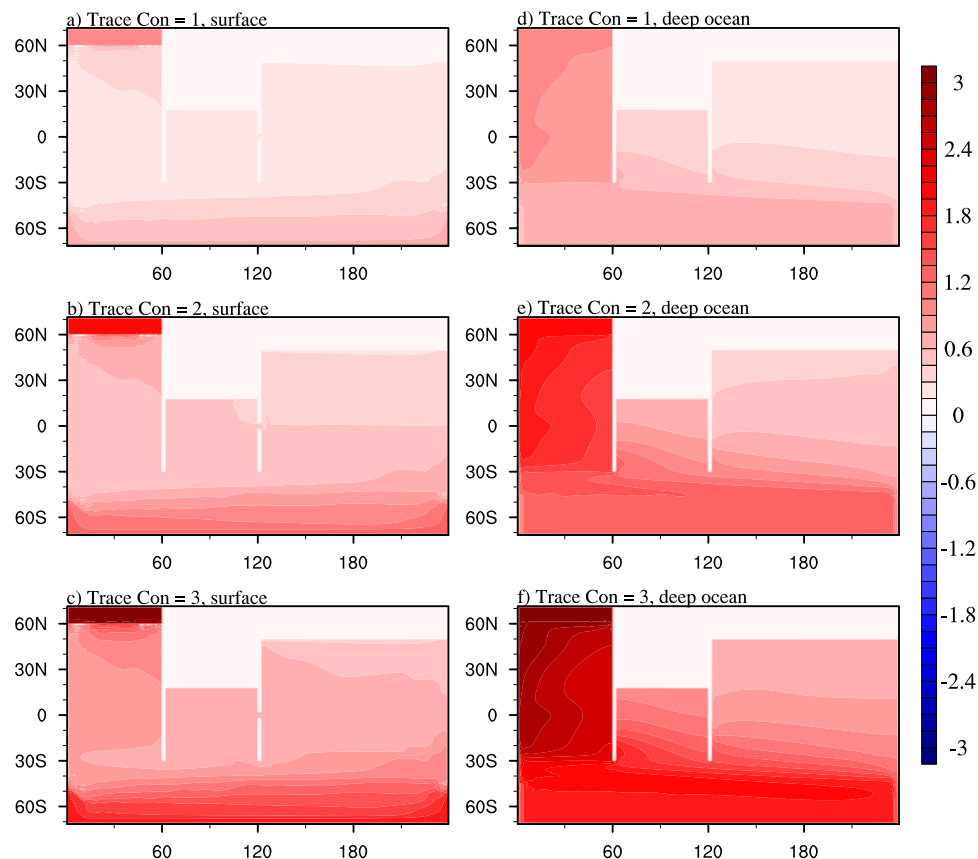


Fig. 6 Tracer concentration in idealized MITgcm experiments. Tracer concentration at the surface (a–c) and in the deep ocean (averaged between 1000–3000 m) (d–f). The concentration of each tracer is relaxed to one (top), two (middle), and three (bottom).

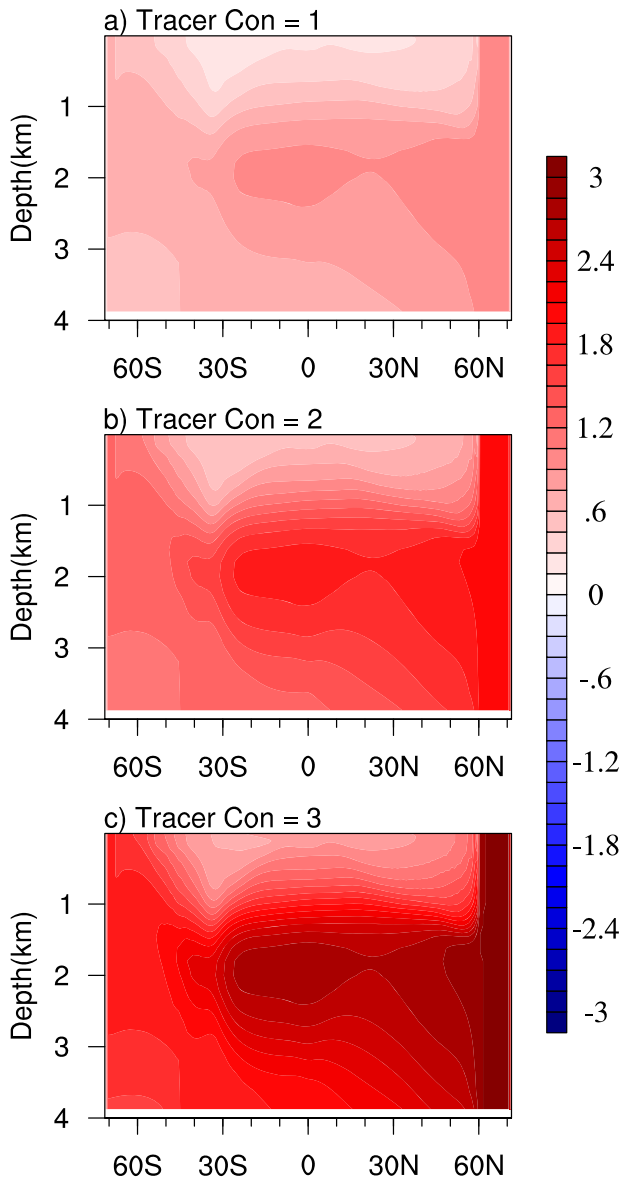


Fig. 7 Zonal-mean tracer concentration in idealized MITgcm experiment. Zonally averaged tracer concentration in the Atlantic Ocean sector for three MITgcm tracer experiments, with tracer concentration relaxed to (a) one, (b) two, (c) three.

which is needed not only for simulating the current climate state, but also for projecting the future climate change.

METHODS

CMIP6 models

Monthly outputs from 18 CMIP6 models in the historical run are used in the present study. The monthly CMIP6 outputs are SST, net shortwave radiation (SW), net longwave radiation (LW), surface latent heat flux (LH), sensible heat flux (SH), sea water potential temperature, salinity, and overturning mass streamfunction. The net surface heat radiation (Q_{net}) is the sum of SW, LW, LH, and SH. For each CMIP6 model, we used only one ensemble member. We prioritized the “r1i1p1f1” ensemble member and selected an alternative member when the preferred member was unavailable. The model names, ensemble members, and institutions are listed

Table 1. List of models and associated information.

Models Names	Ensemble Member	Institute, Country
ACCESS-CM2	r1i1p1f1	CSIRO, Australia
ACCESS-ESM1-5	r1i1p1f1	
CESM2-FV2	r1i1p1f1	NCAR, USA
CESM2-WACCM-FV2	r1i1p1f1	
CESM2-WACCM	r1i1p1f1	
CESM2	r1i1p1f1	
EC-Earth3-Veg	r1i1p1f1	Europe-wide consortium
EC-Earth3	r1i1p1f1	
FGOALS-f3-L	r1i1p1f1	CAS, China
FGOALS-g3	r1i1p1f1	
GISS-E2-1-G	r1i1p1f1	NASA/GISS, USA
HadGEM3-GC31-LL	r1i1p1f3	MOHC, UK
MIROC-ES2L	r1i1p1f2	JAMSTEC, Japan
MIROC6	r1i1p1f1	
MPI-ESM1-2-HAM	r1i1p1f1	MPI-M, Germany
MPI-ESM1-2-HR	r1i1p1f1	
MPI-ESM1-2-LR	r1i1p1f1	
MRI-ESM2-0	r1i1p1f1	MRI, Japan
ACCESS-OM2	r1i1p1f1	CSIRO, Australia
ACCESS-OM2-025	r1i1p1f1	
CAS-ESM2-0	r1i1p1f1	CAMS, China
CMCC-ESM2	r1i1p1f1	CMCC, Italy
NorESM2-LM	r1i1p1f1	NCC, Norway

in Table 1. The current climatology in CMIP6 models is defined as the 33-year long-term mean during the 1982–2014 period.

Observational datasets

The model outputs are compared against several observational/reanalysis datasets (both called *observations* for simplicity in this study). The SST observation is obtained from the Optimum Interpolation SST (OISSTv2)³⁰. The dynamic sea surface height is extracted from MDT_CNES_CLS13³¹ and the surface heat fluxes (including the LH, SH, LW, and SW) are obtained from seven datasets: the ECMWF Reanalysis v5 (ERA5)³², ECMWF Reanalysis – 40 years (ERA40)³³, NCAR/NCEP Reanalysis (NCEP-NCAR)³⁴, NCEP-DOE AMIP-II reanalysis (NCEP-DOE)³⁵, NCEP Climate Forecast System Reanalysis (NCEP-CFSR)³⁶, the Japanese 55-year Reanalysis (JRA-55)³⁷, and 20th Century Reanalysis (20Cv2c)³⁸. The three-dimensional ocean temperature is extracted from the Simple Ocean Data Assimilation (SODA3.4.2)³⁹, and the AMOC index was obtained from RAPID⁴⁰. The observational datasets are detailed in Table 2. Note that the time periods of some observational datasets (such as ERA40, JRA55, and NCEP-CFSR) are slightly different from each other (see Table 2). The main conclusions are not sensitive to the observational datasets being used. In this study, the ACC fronts are defined based on the observed dynamic sea-surface height according to Kim and Orsi⁴¹, with the circumpolar SAF associated with 0.985 dym isoline and the SACCf with -0.035 dym isoline, respectively. The sign of surface heat flux terms is positive when going downward. All model outputs and observational datasets are interpolated into a $2.5^\circ \times 2.5^\circ$ grid before analyses.

Idealized experiments

To verify whether the SO warm SST bias can be attributed to the warm bias in the Northern Atlantic, we employ an ocean model with idealized-geometry based on the Massachusetts Institute of

Table 2. List of observational/reanalysis datasets.

Observation/Reanalysis Datasets	Variables	Time Span
OISSTv2	SST	1982.01–2014.12
MDT_CNES_CLS13	MDT	1993.01–2012.12
ERA5/NCEP-NCAR/NCEP-DOE/20Cv2c	SW/LW/LH/SH	1982.01–2014.12
ERA40	SW/LW/LH/SH	1982.01–2001.11
JRA-55	SW/LW/LH/SH	1982.01–2013.12
NCEP-CFSR	SW/LW/LH/SH	1982.01–2010.12
SODA3.4.2	Ocean Temperature and Salinity	1982.01–2014.12
RAPID	AMOC Strength	2005.01–2014.12
WOA2018	Dissolved Oxygen Concentrations	decadal mean

Technology general circulation model (MITgcm)⁴². The simulation domain, with 1° resolution, spans from 71.5°S to 71.5°N in latitude and 240° in longitude. Two continents divide the domain into the Atlantic, Indian, and Pacific Oceans. The SO is represented by a reentrant channel at the southern edge of the domain. In the vertical direction, the ocean is 4000 m deep everywhere except in the Drake Passage (the submarine sill in the SO), which is 2500 m deep. Detailed information on this model setting refers to ref.⁴³. In this study, three passive-tracer experiments were conducted. In the northern Atlantic Ocean (>60°N), the tracer concentrations are relaxed to one, two, and three through the entire water column. In each case, the simulation runs for 1000 years, sufficient to reach equilibrium. The model outputs are averaged over the last 30 years of simulation for analysis.

DATA AVAILABILITY

The CMIP6 model outputs are archived at the Earth System Grid Federation (<https://esgf-node.llnl.gov/projects/cmip6/>), Monthly sea surface temperature from the OISSTv2 dataset can be downloaded from <https://psl.noaa.gov/data/gridded/data.noaa.oisst.v2.html>. Dynamic topographies (MDT_CNES_CLS13) is from <https://www.aviso.altimetry.fr/en/data/products/auxiliary-products/mdt.html>. ERA5 is from <https://cds.climate.copernicus.eu/cdsapp#!/search?type=dataset&text=ERA5>. ERA40 is from <https://apps.ecmwf.int/datasets/data/era40-moda/levtype=sfc/>. Heat flux products, NCEP-NCAR, NCEP-DOE, and 20Cv2c, are from <https://psl.noaa.gov/data/gridded/reanalysis/>. NCEP-CFSR is from <https://rda.ucar.edu/datasets/ds093.2/dataaccess/>. JRA55 is from <https://climatedataguide.ucar.edu/climate-data/jra-55>. Observational AMOC strength is from https://rapid.ac.uk/rapidmoc/rapid_data/datadl.php. SODA3.4.2 is from https://rapid.ac.uk/rapidmoc/rapid_data/datadl.php. WOA2018 is from <https://www.ncei.noaa.gov/access/world-ocean-atlas-2018/>. The data that support the findings of this study are available at <https://doi.org/10.5281/zenodo.8219810>⁴⁴.

CODE AVAILABILITY

The code used for analysis of this study is available at <https://doi.org/10.5281/zenodo.8219806>⁴⁵.

Received: 28 March 2023; Accepted: 15 August 2023;

Published online: 24 August 2023

REFERENCES

- Marshall, J. & Speer, K. Closure of the meridional overturning circulation through Southern Ocean upwelling. *Nat. Geosci.* **5**, 171–180 (2012).
- Sallee, J. B. Southern Ocean Warming. *Oceanography* **31**, 52–62 (2018).
- Rintoul, S. R. The global influence of localized dynamics in the Southern Ocean. *Nature* **558**, 209–218 (2018).
- Karsten, R. H. & Marshall, J. Constructing the residual circulation of the ACC from observations. *J. Phys. Oceanogr.* **32**, 3315–3327 (2002).
- Talley, L. D. Closure of the global overturning circulation through the Indian, Pacific, and Southern Oceans: schematics and transports. *Oceanography* **26**, 80–97 (2013).
- Sloyan, B. M. & Rintoul, S. R. The Southern Ocean limb of the global deep overturning circulation. *J. Phys. Oceanogr.* **31**, 143–173 (2001).
- Downes, S. M., Bindoff, N. L. & Rintoul, S. R. Impacts of climate change on the subduction of mode and intermediate water masses in the Southern Ocean. *J. Clim.* **22**, 3289–3302 (2009).
- Frölicher, T. L. et al. Dominance of the Southern Ocean in anthropogenic carbon and heat uptake in CMIP5 models. *J. Clim.* **28**, 862–886 (2015).
- Roemmich, D. et al. Unabated planetary warming and its ocean structure since 2006. *Nat. Clim. Change* **5**, 240–245 (2015).
- Bourassa, M. A. et al. High-latitude ocean and sea ice surface fluxes: challenges for climate research. *Bull. Am. Meteorol. Soc.* **94**, 403–423 (2013).
- Sen Gupta, A. et al. Projected changes to the Southern hemisphere ocean and sea ice in the IPCC AR4 climate models. *J. Clim.* **22**, 3047–3078 (2009).
- Wang, C., Zhang, L., Lee, S.-K., Wu, L. & Mechoso, C. R. A global perspective on CMIP5 climate model biases. *Nat. Clim. Change* **4**, 201–205 (2014).
- Farneti, R., Stiz, A. & Ssebendeke, J. B. Improvements and persistent biases in the southeast tropical Atlantic in CMIP models. *npj Clim. Atmos. Sci.* **5**, 42 (2022).
- Hwang, Y.-T. & Frierson, D. M. Link between the double-Intertropical Convergence Zone problem and cloud biases over the Southern Ocean. *Proc. Natl. Acad. Sci. USA* **110**, 4935–4940 (2013).
- Jones, J. M. et al. Assessing recent trends in high-latitude Southern Hemisphere surface climate. *Nat. Clim. Change* **6**, 917–926 (2016).
- Kostov, Y., Ferreira, D., Armour, K. C. & Marshall, J. Contributions of greenhouse gas forcing and the southern annular mode to historical southern ocean surface temperature trends. *Geophys. Res. Lett.* **45**, 1086–1097 (2018).
- Kajtar, J. B. et al. CMIP5 intermodel relationships in the baseline Southern Ocean climate system and with future projections. *Earth's Future* **9**, e2020EF001873 (2021).
- Hyder, P. et al. Critical Southern Ocean climate model biases traced to atmospheric model cloud errors. *Nat. Commun.* **9**, 3625 (2018).
- Eyring, V. et al. Overview of the Coupled Model Intercomparison Project Phase 6 (CMIP6) experimental design and organization. *Geosci. Model Dev.* **9**, 1937–1958 (2016).
- Wild, M. The global energy balance as represented in CMIP6 climate models. *Clim. Dyn.* **55**, 553–577 (2020).
- Weijer, W., Cheng, W., Garuba, O. A., Hu, A. & Nadiga, B. T. CMIP6 models predict significant 21st century decline of the Atlantic meridional overturning circulation. *Geophys. Res. Lett.* **47**, e2019GL086075 (2020).
- Heuzé, C. Antarctic bottom water and north Atlantic deep water in CMIP6 models. *Ocean Sci.* **17**, 59–90 (2021).
- Abernathy, R. & Cessi, P. Topographic enhancement of eddy efficiency in baroclinic equilibration. *J. Phys. Oceanogr.* **44**, 2107–2126 (2014).
- Tamsitt, V. et al. Spiraling pathways of global deep waters to the surface of the Southern Ocean. *Nat. Commun.* **8**, 172 (2017).
- Song, X. et al. Explaining the zonal asymmetry in the air-sea net heat flux climatology over the Antarctic Circumpolar Current. *J. Geophys. Res. Oceans* **125**, e2020JC016215 (2020).
- Beadling, R. L. et al. Representation of Southern Ocean properties across coupled model intercomparison project generations: CMIP3 to CMIP6. *J. Clim.* **33**, 6555–6581 (2020).
- Talley, L. D., Pickard, G. L., Emery, W. J. & Swift, J. H. *Descriptive Physical Oceanography: an Introduction Ch.3*, 47 (Elsevier 2011).
- Messias, M.-J. & Mercier, H. The redistribution of anthropogenic excess heat is a key driver of warming in the North Atlantic. *Commun. Earth Environ.* **3**, 118 (2022).
- Heuzé, C., Heywood, K. J., Stevens, D. P. & Ridley, J. K. Changes in global ocean bottom properties and volume transports in CMIP5 models under climate change scenarios. *J. Clim.* **28**, 2917–2944 (2015).
- Reynolds, R. W., Rayner, N. A., Smith, T. M., Stokes, D. C. & Wang, W. An improved in situ and satellite SST analysis for climate. *J. Clim.* **15**, 1609–1625 (2002).
- Rio, M. H., Mulet, S. & Picot, N. Beyond GOCE for the ocean circulation estimate: synergetic use of altimetry, gravimetry, and in situ data provides new insight into geostrophic and Ekman currents. *Geophys. Res. Lett.* **41**, 8918–8925 (2014).
- Hersbach, H. et al. The ERA5 global reanalysis. *Quat. J. R. Meteorol. Soc.* **146**, 1999–2049 (2020).
- Uppala, S. M. et al. The ERA-40 re-analysis. *Quat. J. R. Meteorol. Soc.* **131**, 2961–3012 (2005).
- Kalnay, E. et al. The NCEP/NCAR 40-Year Reanalysis Project. *Bull. Am. Meteorol. Soc.* **77**, 437–471 (1996).
- Kanamitsu, M. et al. NCEP-DOE AMIP-II Reanalysis (R-2). *Bull. Am. Meteorol. Soc.* **83**, 1631–1643 (2002).

36. Saha, S. et al. The NCEP climate forecast system reanalysis. *Bull. Am. Meteorol. Soc.* **91**, 1015–1057 (2010).
37. Kobayashi, S. et al. The JRA-55 reanalysis: general specifications and basic characteristics. *J. Meteorol. Soc. Jpn. Ser. II* **93**, 5–48 (2015).
38. Compo, G. P. et al. The Twentieth Century Reanalysis Project. *Quat. J. R. Meteorol. Soc.* **137**, 1–28 (2011).
39. Carton, J. A., Chepurin, G. A. & Chen, L. SODA3: a new ocean climate reanalysis. *J. Clim.* **31**, 6967–6983 (2018).
40. Moat, B. I. et al. *Atlantic meridional overturning circulation observed by the RAPID-MOCHA-WBTS (RAPID-Meridional Overturning Circulation and Heatflux Array-Western Boundary Time Series) array at 26N from 2004 to 2020* (British Oceanographic Data Centre - Natural Environment Research Council, UK, 2022); <https://doi.org/10.5285/e91b10af-6f0a-7fa7-e053-6c86abc05a09>.
41. Kim, Y. S. & Orsi, A. H. On the variability of Antarctic Circumpolar Current fronts inferred from 1992–2011 altimetry. *J. Phys. Oceanogr.* **44**, 3054–3071 (2014).
42. Marshall, J., Adcroft, A., Hill, C., Perelman, L. & Heisey, C. A finite-volume, incompressible Navier Stokes model for studies of the ocean on parallel computers. *J. Geophys. Res. Oceans* **102**, 5753–5766 (1997).
43. Sun, S., Thompson, A. F., Xie, S.-P. & Long, S.-M. Indo-Pacific warming induced by a weakening of the Atlantic meridional overturning circulation. *J. Clim.* **35**, 815–832 (2021).
44. Luo, F. Datasets for origins of Southern Ocean warm sea surface temperature bias in CMIP6 models. *Zonodo*, <https://zenodo.org/record/8219810> (2023).
45. Luo, F. Code for origins of Southern Ocean warm sea surface temperature bias in CMIP6 models. *Zonodo*, <https://zenodo.org/record/8219806> (2023).

ACKNOWLEDGEMENTS

We acknowledge the effort of the World Climate Research Program's Working Group on Coupled Modeling, which coordinated and promoted CMIP6. We also thank the climate modeling groups for producing and making available their model output, and the Earth System Grid Federation (ESGF) for archiving the data and providing access. F.L. and J.Y. were supported by the National Natural Science Foundation of China (Grant 42227901), the Scientific Research Fund of the Second Institute of Oceanography, Ministry of Natural Resources (Grand QNYC2001), and the Innovation Group Project of the Southern Marine Science and Engineering Guangdong Laboratory (Zhuhai) (Grant 311021001). T.L. was supported by the National Natural Science Foundation of China (Grant 42106008). D.C. was supported by the National Natural Science Foundation of China (Grant 42227901).

AUTHOR CONTRIBUTIONS

F.L. conceived the study, performed the analysis and wrote the paper. J.Y. and D.C. conceived the study and wrote the paper. T.L. performed the MITgcm passive tracer experiments. All authors discussed the results and interpretation.

COMPETING INTERESTS

The authors declare no competing interests.

ADDITIONAL INFORMATION

Supplementary information The online version contains supplementary material available at <https://doi.org/10.1038/s41612-023-00456-6>.

Correspondence and requests for materials should be addressed to Jun Ying or Dake Chen.

Reprints and permission information is available at <http://www.nature.com/reprints>

Publisher's note Springer Nature remains neutral with regard to jurisdictional claims in published maps and institutional affiliations.



Open Access This article is licensed under a Creative Commons Attribution 4.0 International License, which permits use, sharing, adaptation, distribution and reproduction in any medium or format, as long as you give appropriate credit to the original author(s) and the source, provide a link to the Creative Commons license, and indicate if changes were made. The images or other third party material in this article are included in the article's Creative Commons license, unless indicated otherwise in a credit line to the material. If material is not included in the article's Creative Commons license and your intended use is not permitted by statutory regulation or exceeds the permitted use, you will need to obtain permission directly from the copyright holder. To view a copy of this license, visit <http://creativecommons.org/licenses/by/4.0/>.

© The Author(s) 2023